Reduced spin-Hall effects from magnetic proximity

Wei Zhang, Matthias B. Jungfleisch, Wanjun Jiang, Yaohua Liu,[*] John E. Pearson,
Suzanne G. E. te Velthuis, and Axel Hoffmann

Materials Science Division, Argonne National Laboratory, Argonne, IL 60439, USA

Frank Freimuth and Yuriy Mokrousov

Peter Grünberg Institut and Institute for Advanced Simulation, Forschungszentrum Jülich and JARA, D-52425, Jülich, Germany

Harnessing spin-orbit coupling for the manipulation of spins and magnetization via electric charge currents is the key objective of spin-orbitronics. Towards this end ferromagnetic materials are combined with nonmagnetic materials with strong spin-orbit coupling (typically involving heavy elements). However, many of the nominally nonmagnetic materials are highly susceptible to magnetic proximity effects, and the role of induced moments for spin transport has been controversial. Here we demonstrate that for Pt and Pd increased induced magnetic moments are correlated with strongly reduced spin-Hall conductivities. This observation finds an intuitive explanation in the development of a spin splitting of the chemical potential and the energy dependence of the intrinsic spin-Hall effect determined by first-principles calculations. This work provides simple guidance towards the optimization of spin current efficiencies for devices based on spin-orbit coupling phenomena.

PACS number(s): 72.25.Pn, 75.30.Ds, 75.76.+j

I. INTRODUCTION

The past decade has witnessed the realization that spin-orbit coupling can provide a very efficient pathway for the generation and detection of spin currents. This has given rise to a new paradigm for spintronics, called spin-orbitronics, where the coupling between spin and angular momentum can be used to manipulate magnetizations electrically in metals and insulators [1]. One of the key phenomena is the spin-Hall effect (SHE), which converts a charge current to a spin current [2,3]. Conversely, the inverse spin-Hall effect (ISHE), transforms a spin current into a charge current [4]. The efficiency of this conversion is characterized by a single material-specific parameter, the spin-Hall angle, γ_{SH}, given by the ratio of spin to charge current [5–7]. Experimentally, the spin-Hall angle along with other spin-transport properties are often probed via ISHE and injection of a spin current from ferromagnets (FM) to normal metals (NM) with large spin-orbit coupling, using nonlocal spin valves [8,9], ferromagnetic resonance (spin pumping) [10–15], or temperature gradients (spin-Seebeck effect) [16–18]. To maximize the spin-Hall signal, the thickness of the NM exceeds in most experiments the spin diffusion length, λ_{sf}, of the NM. However, when a thin NM (thickness below λ_{sf}) is placed in contact with a FM, interface effects, such as spin-memory loss [13,19] and magnetic proximity effects [20–24], can become pronounced and alter the spin-transport properties of the sample. Among the materials studied for large spin-Hall effects, Pt and Pd are two of the most popular metals employed, especially Pt, which has been indispensable in the establishment of virtually all the newly discovered pure spin-current phenomena [4,5,9–13,16]. At the same time, both Pt and Pd have been well known to order ferromagnetically with even minute amounts of magnetic impurities [25] and give rise to magnetic proximity effects

———————

*Present address: Quantum Condensed Matter Division, Oak Ridge National Laboratory, Oak Ridge, TN, USA.

in heterostructures [20–22,25–27]. Recently, this started a controversy over whether the proximity effects of Pt and Pd are relevant to many magnetotransport characteristics [28–33]. However, if and how they influence the spin-Hall effects of Pt and Pd has not been established.

In this work, we experimentally study the temperature evolution of spin-Hall effects in permalloy (Py, $Ni_{80}Fe_{20}$)/NM bilayers (NM = Pt or Pd) using spin pumping and ISHE measurements. By focusing on very thin NM, where proximity effects are most pronounced, we observe a significant decrease of the ISHE with decreasing temperature. Furthermore, we show how this observation can be quantitatively understood by the energy dependence of the intrinsic spin-Hall conductivity determined from first-principles calculations.

II. EXPERIMENT

We fabricated the devices using our previous recipe [34]. The key samples are thin Pt (0.6 nm) and thin Pd (3 nm) on top of Py layers (15 nm) respectively, deposited by magnetron sputtering at rates less than 1 Å/s. In order to check the interface characteristics of our samples, we first measured x-ray reflectivities and their analysis yielded roughness values for all relevant interfaces involved in our samples. For x-ray characterization we grew Py (15 nm)/Pt (10 nm), Py (15 nm)/Pd (10 nm), Py (15 nm)/Cu (4 nm)/Pt (10 nm), and Py (15 nm)/Cu (4 nm)/Pd (10 nm) samples. The x-ray data were fitted with the Parratt formalism to determine the depth-dependent scattering length density (SLD) profiles. A rough interface was modeled as a sequence of thin slices with SLD values varying as an error function so as to interpolate between adjacent layers [35]. We found that the roughness is 0.8 nm for both Pt and Pd grown on Py; see Fig. 1 and Table I. In case of Pd, the deposited thickness of the actual sample (3 nm) is greater than the roughness obtained from x-ray study. In the case of Pt, the deposited thickness is comparable to the roughness, indicating that the Pt layer
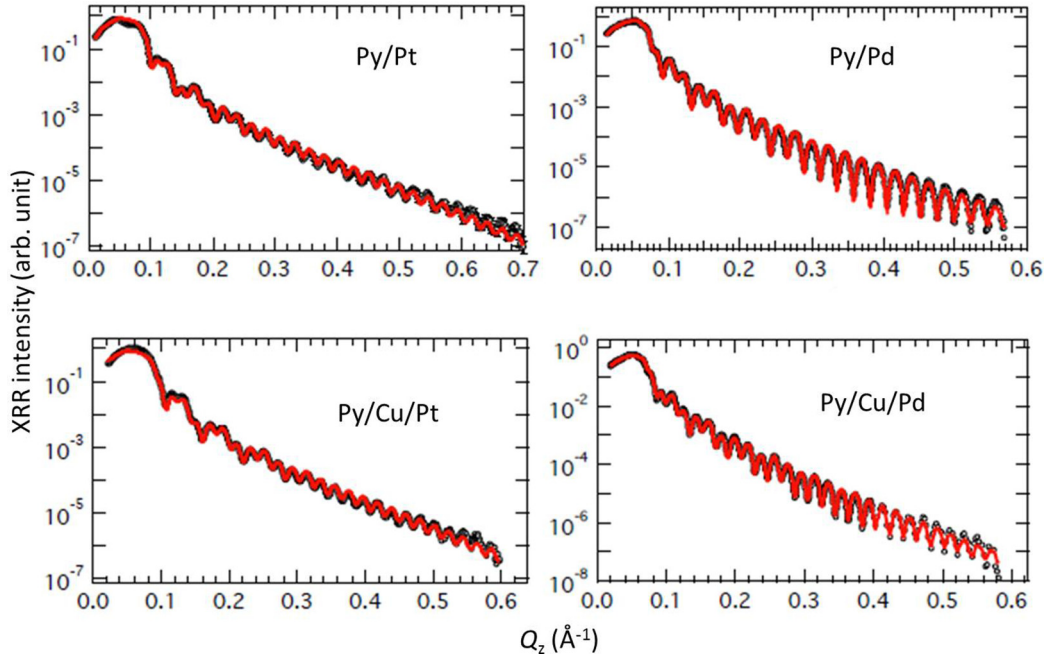
FIG. 1. (Color online) X-ray reflectivity data for Py/Pt(Pd) and Py/Cu/Pt(Pd) samples and the corresponding fittings for determining the roughness values.

may be subject to enhanced surface scattering. However, this surface scattering does not alter the conclusion of our present work, as is discussed later.

The spin pumping samples were patterned in the shape of 20 μm $\times$ 2 mm stripes using lithography on Si substrates with 300-nm-thick thermally grown SiO$_2$. Electrical leads and a coplanar waveguide (CPW) were subsequently fabricated [Fig. 2(a)]. A 80-nm-thick MgO spacer was used to separate the bilayer stack from the CPW. The measuring frequency was kept between 4 and 6 GHz and the rf power was 10 mW.

III. EXPERIMENTAL RESULTS AND DISCUSSIONS

Figures 2(b) and 2(c) illustrate the dc voltages measured at 4 GHz for Py/Pt and Py/Pd at selective temperatures. By generating macroscopic spin currents and using an amplitude-modulated lock-in detection, we probe dc voltages of tens of μV and obtain clearly distinguishable complex-Lorentzian lineshapes. The signals have superimposed symmetric and antisymmetric Lorentzian components. The antisymmetric component is due to the homodyne anisotropic magnetoresistance (AMR) while the symmetric component originates

TABLE I. Calculated roughness values for each interface of the x-ray samples measured in Fig. 1 (units in nm, Vac = vacuum).

	Py/Pt	Py/Cu/Pt	Py/Pd	Py/Cu/Pd
Py/SiO$_2$	0.34	0.38	0.27	0.33
Cu/Py	n/a	0.76	n/a	0.61
Pt(Pd)/Cu	n/a	0.76	n/a	0.61
Pt(Pd)/Py	0.86	n/a	0.81	n/a
Vac/Pt(Pd)	0.31	0.34	0.44	0.49

from the ISHE. Unintentional temperature gradients can give rise to an anomalous Nernst voltage with a symmetric component [36], which we avoid in our samples using a design with a thick high-thermal-conductivity layer above and an even thicker substrate below. The pure AMR-type signal in a pure Py sample [34] demonstrates the absence of both anomalous Nernst effect and the self-induced ISHE voltage of Py [37,38]. In Figs. 2(b) and 2(c), a reduction of the ISHE component with respect to the AMR is observed with decreasing temperature for both Pt and Pd. Since both ISHE and AMR originate from the rf-driven magnetization precession, both effects have the same rf-power dependence and the resultant dc voltage is a sum of the two [34,39]. We define W_{ISHE} as the weight of the symmetric component (ISHE), which can be expressed in the form of $W_{\text{ISHE}} = 1/(1 + V_{\text{AMR}}/V_{\text{ISHE}})$. The ratio of the two components can be written as [34]

$$\frac{V_{\text{ISHE}}}{V_{\text{AMR}}} = \frac{\gamma_{\text{SH}} e L P f g_{\text{mix}} \lambda_{sf}}{R_{\text{CPW}} I_{\text{CPW}} \frac{\Delta R_{\text{FM}}}{R_{\text{FM}}}} \frac{h_{rf}}{\Delta H} \frac{\rho_{\text{FM}}}{t_{\text{FM}}} \tanh\left(\frac{t_{\text{NM}}}{2\lambda_{sf}}\right), \quad (1)$$

where γ_{SH} is the spin-Hall angle, L is the device length, P is an ellipticity correction, R_{CPW} is the CPW resistance, I_{CPW} is the CPW current, $\frac{\Delta R_{\text{FM}}}{R_{\text{FM}}}$ is the FM anisotropic magnetoresistance, h_{rf} is the rf field, ΔH is the linewidth, and ρ_{FM} is the FM resistivity [34]. In Eq. (1), only the spin-Hall angle, γ_{SH}, the spin mixing conductance, g_{mix}, the spin diffusion length, λ_{sf}, and the normal metal layer thickness, t_{NM}, are dependent on the NM. Therefore, W_{ISHE} can be rewritten as

$$W_{\text{ISHE}} = \left(1 + \frac{1}{C\gamma_{\text{SH}} g_{\text{mix}} \lambda_{sf} \tanh\left(\frac{t_{\text{NM}}}{2\lambda_{sf}}\right)}\right)^{-1}, \quad (2)$$

where C depends on f due to changing P of the precession [40,41] and is otherwise only a function of the CPW and FM layer.
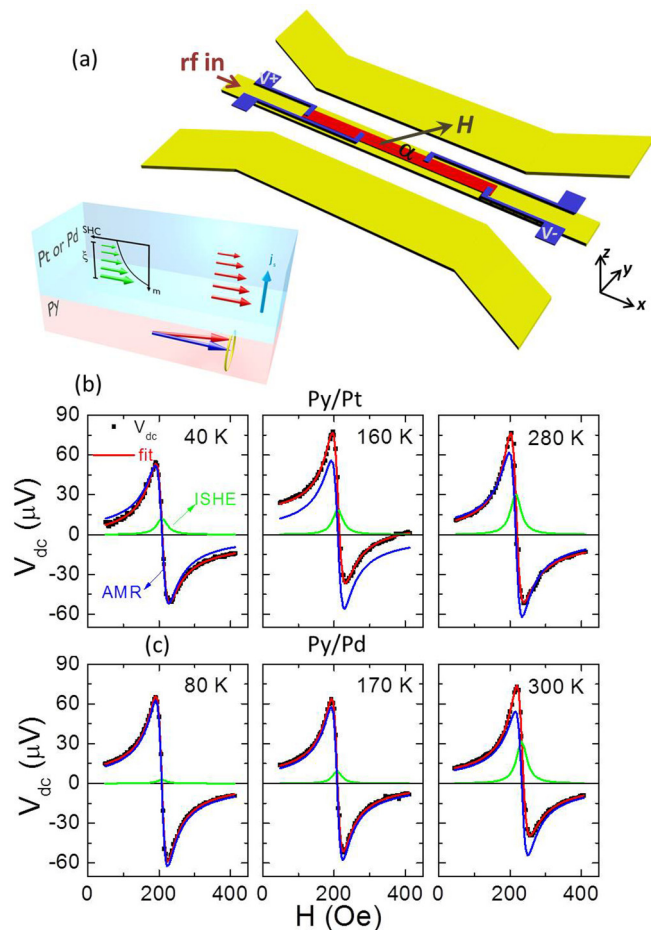
FIG. 2. (Color online) (a) Schematic illustration of the spin pumping and ISHE experiments showing the respective polarity (rf input, external field, H, and dc voltage contacts, V_+/V_-), and the external field direction, $\alpha = 40^\circ$ with respect to the central signal line. Due to magnetic proximity effect, the spin-Hall conductivities (SHC) are reduced near the interface, since they are functions of induced magnetic moments that decay away from the interface within a very thin thickness range; these effects are observed by ISHE measurements only for very thin layers of Pt and Pd on top of Py. AMR-ISHE spectra measured at 4 GHz for (b) Py/Pt and (c) Py/Pd at selective temperatures.

Figure 3 shows the spin pumping data for two reference samples, i.e., Py (15 nm)/Cu (4 nm)/Pt (0.6 nm) and Py (15 nm)/Cu (4 nm)/Pd (3 nm) at selective temperatures. The additional 4-nm Cu spacer in the Py/Cu/NM samples blocks any possible spin interface effects, while it only weakly changes the spin current transport due to the long spin diffusion length of Cu [42]. The symmetric component from ISHE is clearly separated from the asymmetric component that arises from the AMR in the spectrum. No pronounced decay of the ISHE signal is observed for both Pt and Pd. Figure 4 summarizes the temperature dependence of W_{ISHE} values for Pt and Pd with and without a Cu spacer. We note that x-ray reflectivity shows similar roughness for the Pt and Pd layers with and without the Cu interlayer, suggesting that possible changes in microstructure are inconsequential (Fig. 1). We also note that the Cu layer may change other interfacial
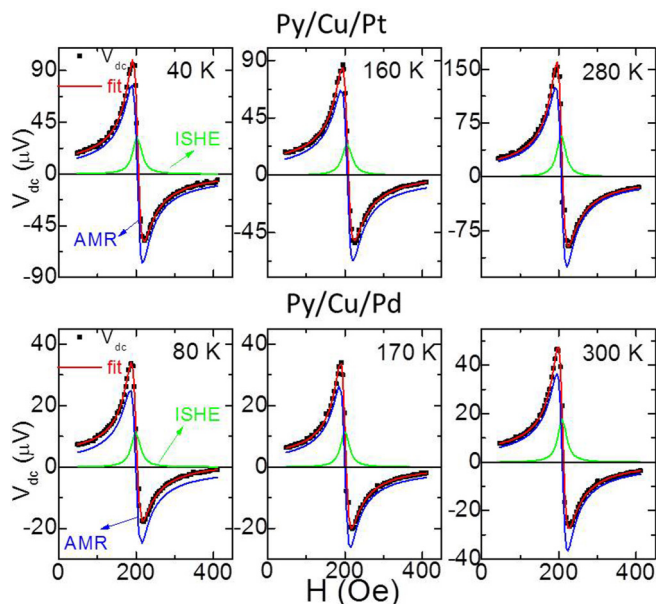

FIG. 3. (Color online) DC voltage spectra measured at 4 GHz for Py/Cu/Pt and Py/Cu/Pd reference samples at selective temperatures.

contributions to the measured signals (e.g., from Rashba interactions), if there exists a strong spin-orbit coupling at the interface between Py and Pt(Pd) in addition to SHE. However, the W_{ISHE} ratio for samples with and without Cu spacer show similar values (Fig. 4), indicating that such interface effects are negligible at room temperature (RT); it also indicates the weak dependence of spin pumping and ISHE detection on the insertion of the thin Cu layer, since electric current shunting is expected to reduce both the spin Hall and anisotropic magnetoresistance signals in the same way. In order to
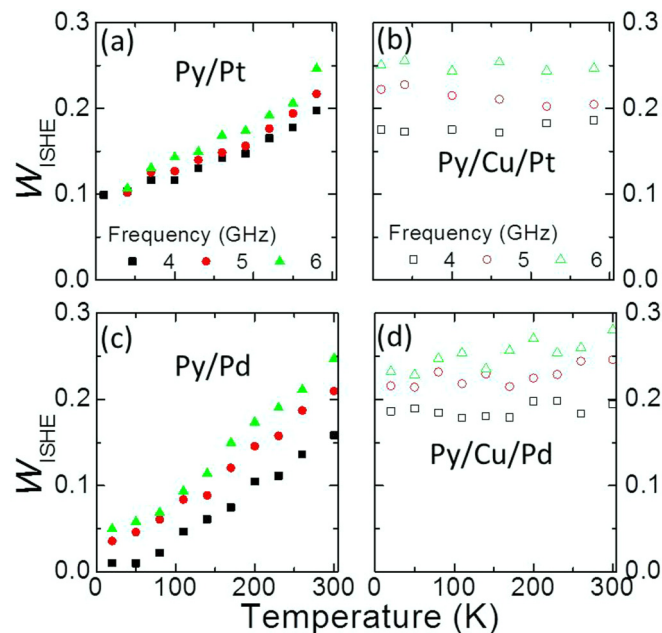

FIG. 4. (Color online) Temperature dependence of W_{ISHE} at 4, 5, and 6 GHz for (a) Py/Pt, (b) Py/Cu/Pt, (c) Py/Pd, and (d) Py/Cu/Pd bilayers.
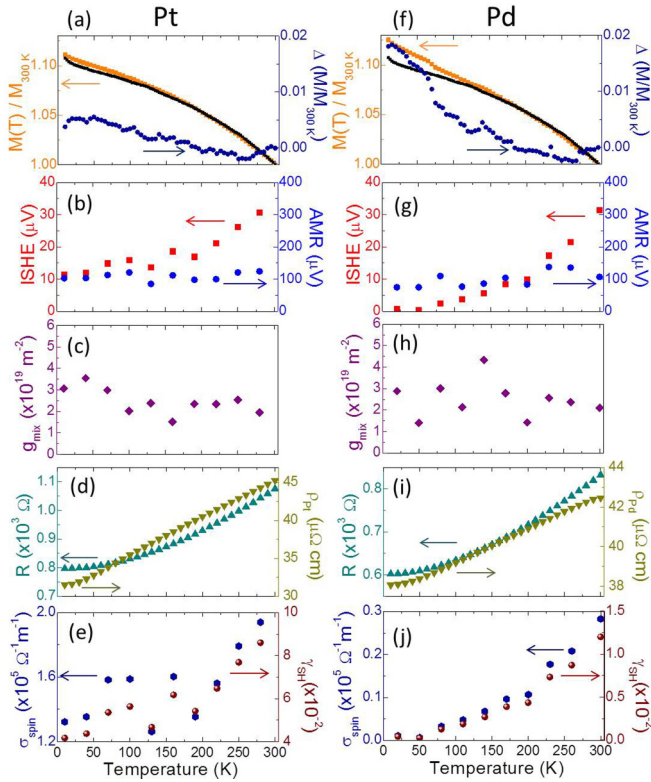
FIG. 5. (Color online) Temperature dependence of (a) normalized magnetization, $M(T)/M_{300K}$ (with respect to 300 K) of Py/Pt and Py and their differences (Δ), measured by a SQUID magnetometry with 2k Oe in-plane applied field. (b) AMR and ISHE voltage amplitudes at 4 GHz, (c) spin mixing conductance, (d) device total resistance and Pt resistivity, and (e) calculated spin-Hall angle and spin-Hall conductivity for Pt. Right panels (f)–(j) are corresponding results for Pd.

possibly explain the strong temperature dependence at low temperatures, this would require in Py/Pt(Pd) a Rashba-type contribution with opposite sign to the spin Hall effect [43], which also increases with decreasing temperature.

The value of W_{ISHE} strongly decreases with decreasing temperature in Py/NM samples, while it remains almost temperature independent for Py/Cu/NM samples. The nearly constant W_{ISHE} for Py/Cu/NM indicates a weak temperature dependence of the intrinsic SHE (γ_{SH}, g_{mix}, and λ_{sf}) for paramagnetic Pt and Pd, which has also been found using lateral spin valves [44], spin Hall magnetoresistance [45], and first-principles calculations [46]. In contrast, we attribute the observed strong temperature dependence in Py/NM bilayers to a temperature-dependent proximity effect of magnetically ordered Pt and Pd. This magnetic proximity arises at the Py/NM interface and reduces the effective spin Hall angle (which is apparent from the decreasing of the ratio W_{ISHE} with temperature, Fig. 4). Figures 5(a) and 5(f) show the normalized magnetization versus temperature measured with a superconducting quantum interference device (SQUID, Quantum Design) for extended Py/Pt and Py/Pd samples compared to a Py reference sample. For both Pt and Pd there is an additional net magnetization, which becomes more

pronounced at low temperatures. This is consistent with a temperature-dependent proximity effect.

Two competing length scales are important in this context: (1) the spin diffusion lengths of the spin current and (2) the correlation length of the proximity effect, ξ. In our previous studies, we determined the spin diffusion length of Pt (1.2 nm) [34] and Pd (5.5 nm) [39], which is nearly a temperature-independent parameter [34,45]. However, in these studies we investigated thicker layers ($t_{NM} > 1$ nm) and it was shown that W_{ISHE} for Pt is almost the same at RT and 10 K. These results imply that the correlation length is on the order of less than 1 nm for Pt at 10 K and less than 3 nm for Pd from our present work. Strong temperature-dependent ξ has been reported in Py/Pt [31], YIG/Pt [47], and YIG/Pd [32,48], with $\xi \sim 0.8$ nm for Pt [31] and $\xi \sim 2$ nm for Pd [32] at low temperatures. We suggest that the observed reduction of the SHE in thin Pt and Pd is due to a temperature-dependent magnetic proximity effect obvious from a strong variation of the ratio ξ/λ_{sf} with temperature.

In order to quantify the temperature-dependent spin Hall angle of the thin Pt and Pd, we distinguish the absolute values of the two voltage components. Figures 5(b) and 5(g) show the temperature dependences of ISHE and AMR voltages obtained at 4 GHz for Pt and Pd respectively, which confirm that the decreasing W_{ISHE} is purely due to the decreased ISHE. We also extract the effective spin mixing conductance from the damping enhancement due to spin pumping, $\Delta\alpha$ [Figs. 2(b) and 2(c)], according to [10,13,39]

$$g_{mix} = \frac{4\pi M_s t_{FM}}{g\mu_B}\Delta\alpha, \qquad (3)$$

where g, μ_B, and M_s are the Landé g factor, Bohr magneton, and saturation magnetization of Py, respectively. We do not observe any appreciable temperature dependence of g_{mix} [Figs. 5(c) and 5(h)]. The spin-Hall angle can be estimated via [10,39]

$$V_{ISHE} = R\gamma_{SH}ewPfg_{mix}\sin\alpha\sin^2\theta\lambda_{sf}\tanh\left(\frac{t_{NM}}{2\lambda_{sf}}\right), \quad (4)$$

where w is the stripe width and R is the total bilayer resistance, which is directly measured; see Figs. 5(d) and 5(i). Using these values, the spin-Hall angles at different temperatures are estimated [Figs. 5(e) and 5(j)] by assuming a temperature-independent precession cone-angle, θ, g_{mix}, and λ_{sf}. For Pt, the spin-Hall angle decreases from 0.086 at RT [34] to 0.042 at 10 K, i.e., more than a factor of 2; for Pd, we found nearly negligible SHE at low temperatures as compared to a spin Hall angle at RT of 0.012 [39]. This result indicates a more pronounced proximity effect for Pd than for Pt. We also calculate the temperature-dependent SHE conductivity σ_{spin} from the relation $\gamma_{SH} = \sigma_{spin}/\sigma$, where σ is the electrical conductivity of NMs, $\sigma = \rho^{-1}$. Furthermore, we estimate the resistivity of thin Pt and Pd layers from independent samples (2-nm Pt and 3-nm Pd) using four-point measurements. For Pt, the SHE conductivity reduces from $(1.9 \pm 0.2) \times 10^5 \Omega^{-1} m^{-1}$ at RT to $(1.3 \pm 0.2) \times 10^5 \Omega^{-1} m^{-1}$ at 10 K; for Pd, it is $(0.3 \pm 0.1) \times 10^5 \Omega^{-1} m^{-1}$ and almost negligible (below our detection limit) at $T < 80$ K. It is noted that our samples may be subjected to enhanced surface scattering due to the thin layers of Pt and Pd; however, such fact would not alter

our conclusion. On one hand, it is the total device resistance, instead of the independently characterized resistivity, that dictates the measured spin Hall voltages [Eq. (4)]. On the other hand, this surface scattering would only increase the resistivity of Pt and also makes its temperature dependence less significant. Therefore, the spin-Hall conductivity values at lower temperatures may be overestimated in our case, implying an even stronger reduction of spin-Hall effects due to the magnetic proximity effect. Finally, we found that the roughnesses for Pt and Pd grown on Cu show comparable but slightly reduced values (Fig. 1), indicating a smoother interface between Cu and Pt (Pd).

IV. FIRST-PRINCIPLES CALCULATIONS

In order to assess the influence of the proximity-induced moment, we calculated the SHE conductivity of magnetized bulk fcc Pt and Pd from first principles. We determined the electronic structure of paramagnetic Pt and Pd within the generalized gradient approximation (GGA) to density functional theory [49]. The calculations were performed with the full-potential linearized augmented-plane-wave code FLEUR [50]. In order to minimize the computational cost, we made use of Wannier interpolation [51]. We constructed 18 maximally localized Wannier functions [52,53] per atom describing the $5s$, $4d$, and $5p$ states in Pd and the $6s$, $5d$, and $6p$ states in Pt. Using the electronic structure of the paramagnetic bulk elements represented in the Wannier function basis, we evaluated the intrinsic SHE conductivity

$$\sigma_{\text{spin}}(E) = \frac{-4e^2}{N} \sum_{\mathbf{k}} \sum_{\epsilon_{\mathbf{k}n} < E < \epsilon_{\mathbf{k}m}} \text{Im} \frac{\langle \mathbf{k}n | Q_x^z | \mathbf{k}m \rangle \langle \mathbf{k}m | v_y | \mathbf{k}n \rangle}{(\epsilon_{\mathbf{k}n} - \epsilon_{\mathbf{k}m})^2}$$

(5)

as a function of chemical potential E. Here, N is the number of k points $\mathbf{k}$, $\epsilon_{\mathbf{k}n}$ is the band energy, v_y is the y component of velocity, and $Q_x^z = \frac{\hbar}{4V}[\sigma_z v_x + v_x \sigma_z]$ is the spin current density with V the unit cell volume and σ_z a Pauli matrix. A $800 \times 800 \times 800$ Monkhorst-Pack k mesh [54] was employed to sample the Brillouin zone. The SHE conductivity with a proximity-induced spin magnetic moment μ is estimated as $\sigma_{\text{spin}} = [\sigma_{\text{spin}}(E_\uparrow) + \sigma_{\text{spin}}(E_\downarrow)]/2$, where $E_\uparrow$ and $E_\downarrow$ are determined from $\mu = n(E_\downarrow) - n(E_\uparrow)$ and $2n(E_F) = n(E_\uparrow) + n(E_\downarrow)$, where $2n(E)$ is the number of states with energy lower than E in the paramagnetic system, and $2n(E_F) = 10$ is the number of valence electrons. In Figs. 6(a) and 6(b) we show the SHE conductivity as a function of chemical potential for the paramagnetic case. In the case of Pt, a pronounced maximum is located at $E = E_F$. The chemical potential dependence in Pd is very similar to the Pt case but the maximum is shifted to roughly 0.3 eV below E_F. Since both Pt and Pd have their Fermi level close to the maximum of the SHE conductivity, spin-dependent changes of the band structure, which are akin to a spin splitting of the chemical potential upon the development of a net magnetic moment, lead to a reduction of SHEs.

Figures 6(c) and 6(d) show the calculated SHE conductivity in the presence of an induced spin magnetic moment. Due to the maximum of the SHE conductivity at $E = E_F$ for Pt, the SHE conductivity decreases significantly with increasing
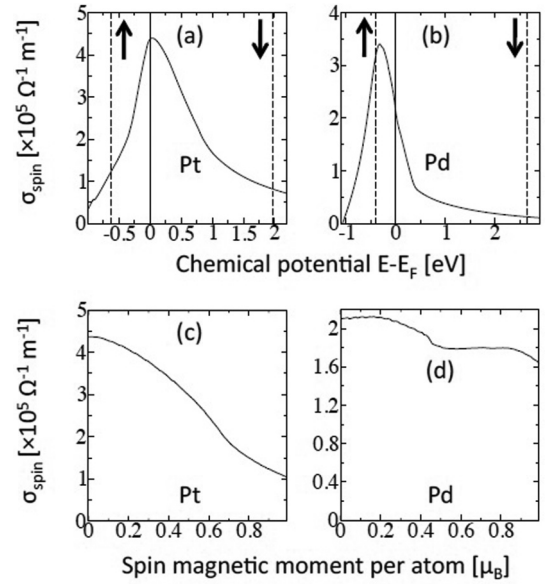

FIG. 6. Panels (a) and (b): Chemical potential dependence of the intrinsic SHE conductivity in Pt and Pd. The dashed lines indicate the spin-Hall conductivities $\sigma_{\text{spin}}(E_\downarrow)$ of the majority spins and $\sigma_{\text{spin}}(E_\uparrow)$ of the minority spins in a spin-polarized system with an induced moment of 1 μ_B. Panels (c) and (d): Estimated dependence of the intrinsic SHE conductivity on the proximity-induced spin magnetic moment.

moment μ in Fig. 6(c). In contrast, the induced-moment dependence of the SHE in Pd shown in Fig. 6(d) is much weaker because the maximum of the SHE conductivity in Fig. 6(b) is shifted to 0.3 eV below E_F. In the absence of a spin magnetic moment in Pt we obtain $\sigma_{\text{spin}} = 4.37 \times 10^5 \Omega^{-1} \text{m}^{-1}$, which compares satisfactorily with $\sigma_{\text{spin}} = 1.9 \times 10^5 \Omega^{-1} \text{m}^{-1}$ measured experimentally at RT. However, the experimental RT value of $\sigma_{\text{spin}} = 0.3 \times 10^5 \Omega^{-1} \text{m}^{-1}$ in Pd is considerably smaller than the theoretical value of $\sigma_{\text{spin}} = 2.1 \times 10^5 \Omega^{-1} \text{m}^{-1}$ at $\mu = 0$. The relatively large difference in the case of Pd might result from shortcomings of the electronic structure obtained from the GGA [55]. Furthermore, additional extrinsic mechanisms might contribute to SHE and reduce the SHE angle if they are opposite to the intrinsic mechanism considered here. Experimentally the SHE conductivity in Pt reduces by 32% from RT to 20 K, which can be explained theoretically by an increase of the induced Pt moment by 0.5 μ_B [see Fig. 6(c)]. This is similar to values found with element-specific x-ray magnetic dichroism measurements finding values of induced Pt moment per atom to be 0.1–0.3 μ_B in Ni/Pt [21], 0.7 μ_B in Co/Pt [26], and 0.5 μ_B in Fe/Pt [27]. In addition, through thickness studies, such a proximity-induced magnetization is found to be maintained for Pt thickness up to 1 nm. Thus for Pt this simple picture with a temperature-dependent proximity-induced magnetization explains quantitatively the observed reduction of the SHE.

On the other hand, the situation in Pd appears to be more complex. The theoretical reduction of the SHE in Pd by an induced moment as shown in Fig. 6(d) underestimates the relative reduction seen in experiment. As discussed above we may not sufficiently accurately capture the

electronic structure within the GGA. An alternative explanation is the presence of an additional external SHE contribution of opposite sign. Interestingly, the absolute change of SHE between RT and 20 K of $0.3 \times 10^5 \Omega^{-1} \mathrm{m}^{-1}$ does compare to the absolute reduction by $0.29 \times 10^5 \Omega^{-1} \mathrm{m}^{-1}$ between $\mu = 0$ and $\mu = 0.5 \mu_B$ [see Fig. 6(d)], suggesting that a temperature-independent offset by $1.8 \times 10^5 \Omega^{-1} \mathrm{m}^{-1}$ due to an additional extrinsic mechanism might explain the discrepancy between experiment and theory.

the results for Pd may require additional investigations for their detailed understanding. Nevertheless, the straightforward explanation of the induced moment dependence of the spin-Hall effect by a spin splitting of the chemical potential together with the energy dependence of the spin Hall conductivity provides a general pathway for estimating the influence of proximity effects in arbitrary materials. Therefore this will help in designing magnetic multilayers for maximum spin current efficiency in spin-orbitronics device concepts.

V. CONCLUSIONS

In summary, we showed the temperature-dependent spin pumping and inverse spin-Hall effects in thin Pt and Pd layers in direct contact with Py. We observe a pronounced decrease of the spin-Hall effect with decreasing temperature, which is attributed to a temperature-dependent proximity effect. By first-principles calculations, we show that the spin-Hall conductivity reduces by increasing the proximity-induced spin magnetic moments. While the experimental observation for Pt is quantitatively consistent with the theoretical calculations,

ACKNOWLEDGMENTS

[1] A. Hoffmann and H. Schultheiß, Mesoscale magnetism, Curr. Opin. Solid State Mat. Sci. (2014).

[2] M. I. D'yakonov and V. I. Perel, Possibility of orienting electron spins with current, Sov. Phys. JETP Lett. **13**, 467 (1971).

[3] J. E. Hirsch, Spin Hall effect, Phys. Rev. Lett. **83**, 1834 (1999).

[4] E. Saitoh, M. Ueda, H. Miyajima, and G. Tatara, Conversion of spin current into charge current at room temperature: Inverse spin-Hall effect, Appl. Phys. Lett. **88**, 182509 (2006).

[5] A. Hoffmann, Spin Hall effects in metals, IEEE Trans. Magn. **49**, 5172 (2013).

[6] L. Liu, C.-F. Pai, Y. Li, H. W. Tseng, D. C. Ralph, and R. A. Buhrman, Spin-torque switching with the giant spin Hall effect of tantalum, Science **336**, 555 (2012).

[7] W. Zhang, M. B. Jungfleisch, W. Jiang, J. Sklenar, F. Y. Fradin, J. E. Pearson, J. B. Ketterson, and A. Hoffmann, Spin pumping and inverse spin Hall effects-Insights for future spin-orbitronics, J. Appl. Phys. **117**, 172610 (2015).

[8] S. O. Valenzuela and M. Tinkham, Direct electronic measurement of the spin Hall effect, Nature (London) **442**, 176 (2006).

[9] T. Kimura, Y. Otani, T. Sato, S. Takahashi, and S. Maekawa, Room-temperature reversible spin Hall effect, Phys. Rev. Lett. **98**, 156601 (2007).

[10] O. Mosendz, J. E. Pearson, F. Y. Fradin, G. E. W. Bauer, S. D. Bader, and A. Hoffmann, Quantifying spin Hall angles from spin pumping: Experiments and theory, Phys. Rev. Lett. **104**, 046601 (2010).

[11] F. D. Czeschka, L. Dreher, M. S. Brandt, M. Weiler, M. Althammer, I.-M. Imort, G. Reiss, A. Thomas, W. Schoch, W. Limmer, H. Huebl, R. Gross, and S. T. B. Goennenwein, Scaling behavior of the spin pumping effect in ferromagnet-platinum bilayers, Phys. Rev. Lett. **107**, 046601 (2011).

[12] A. Azevedo, L. H. Vilela-Leão, R. L. Rodriguez-Suarez, A. F. Lacerda Santos, and S. M. Rezende, Spin pumping and

anisotropic magnetoresistance voltages in magnetic bilayers: Theory and experiment, Phys. Rev. B **83**, 144402 (2011).

[13] J. C. Rojas-Sanchez *et al.*, Spin pumping and inverse spin Hall effect in platinum: The essential role of spin-memory loss at metallic interfaces, Phys. Rev. Lett. **112**, 106602 (2014).

[14] H. L. Wang, C. H. Du, Y. Pu, R. Adur, P. C. Hammel, and F. Y. Yang, Scaling of spin Hall angle in 3d, 4d, and 5d metals from $Y_3Fe_5O_{12}$/metal spin pumping, Phys. Rev. Lett. **112**, 197201 (2014).

[15] W. Zhang, M. B. Jungfleisch, W. Jiang, J. E. Pearson, A. Hoffmann, F. Freimuth, and Y. Mokrousov, Spin Hall effects in metallic antiferromagnets, Phys. Rev. Lett. **113**, 196602 (2014).

[16] K. Uchida, S. Takahashi, K. Harii, J. Ieda, W. Koshibae, K. Ando, S. Maekawa, and E. Saitoh, Observation of the spin Seebeck effect, Nature (London) **455**, 778 (2008).

[17] C. M. Jaworski, J. Yang, S. Mack, D. D. Awschalom, J. P. Heremans, and R. C. Myers, Observation of the spin-Seebeck effect in a ferromagnetic semiconductor, Nat. Mater. **9**, 898 (2010).

[18] D. Qu, S. Y. Huang, J. Hu, R. Wu, and C. L. Chien, Intrinsic spin seebeck effect in Au/YIG, Phys. Rev. Lett. **110**, 067206 (2013).

[19] H. Kurt, R. Loloee, K. Eid, W. P. Pratt, Jr., and J. Bass, Spin-memory loss at 4.2 K in sputtered Pd and Pt and at Pd/Cu and Pt/Cu interfaces, Appl. Phys. Lett. **81**, 4787 (2002).

[20] G. Bergmann, Transition from Pauli paramagnetism to band ferromagnetism in very thin Ni films, Phys. Rev. Lett. **41**, 264 (1978).

[21] F. Wilhelm *et al.*, Layer-resolved magnetic moments in Ni/Pt multilayers, Phys. Rev. Lett. **85**, 413 (2000).

[22] J. Vogel, A. Fontaine, V. Cros, F. Petroff, J.-P. Kappler, G. Krill, A. Rogalev, and J. Goulon, Structure and magnetism of Pd in Pd/Fe multilayers studied by x-ray magnetic circular dichroism at the Pd $L_{2,3}$ edges, Phys. Rev. B **55**, 3663 (1997).

[23] K.-S. Ryu, S. H. Yang, L. Thomas, and S. S. P. Parkin, Chiral spin torque arising from proximity-induced magnetization, Nat. Commun. **5**, 3910 (2014).

[24] G. Y. Guo, Q. Niu, and N. Nagaosa, Anomalous Nernst and Hall effects in magnetized platinum and palladium, Phys. Rev. B **89**, 214406 (2014).

[25] J. Crangle and W. R. Scott, Dilute ferromagnetic alloys, J. Appl. Phys. **36**, 921 (1965).

[26] F. Wilhelm *et al.*, Interface magnetism in 3d/5d multilayers probed by x-ray magnetic circular dichroism, Phys. Status Solidi A **196**, 33 (2003).

[27] W. J. Antel *et al.*, Induced ferromagnetism and anisotropy of Pt layers in Fe/Pt(001) multilayers, Phys. Rev. B **60**, 12933 (1999).

[28] S. Y. Huang, X. Fan, D. Qu, Y. P. Chen, W. G. Wang, J. Wu, T. Y. Chen, J. Q. Xiao, and C. L. Chien, Transport magnetic proximity effects in platinum, Phys. Rev. Lett. **109**, 107204 (2012).

[29] Y. Sun *et al.*, Damping in yttrium iron garnet nanoscale films capped by platinum, Phys. Rev. Lett. **111**, 106601 (2013).

[30] S. Shimizu, K. S. Takahashi, T. Hatano, M. Kawasaki, Y. Tokura, and Y. Iwasa, Electrically tunable anomalous Hall effect in Pt thin films, Phys. Rev. Lett. **111**, 216803 (2013).

[31] W. L. Lim, N. Ebrahim-Zadeh, J. C. Owens, H. G. E. Hentschel, and S. Urazhdin, Temperature-dependent proximity magnetism in Pt, Appl. Phys. Lett. **102**, 162404 (2013).

[32] T. Lin, C. Tang, and J. Shi, Induced magneto-transport properties at palladium/yttrium iron garnet interface, Appl. Phys. Lett. **103**, 132407 (2013).

[33] B. F. Miao *et al.*, Physical origins of the new magnetoresistance in Pt/YIG, Phys. Rev. Lett. **112**, 236601 (2014).

[34] W. Zhang, V. Vlaminck, J. E. Pearson, R. Divan, S. D. Bader, and A. Hoffmann, Determination of the Pt spin diffusion length by spin-pumping and spin Hall effect, Appl. Phys. Lett. **103**, 242414 (2013).

[35] Y. Liu, S. G. E. te Velthuis, J. S. Jiang, Y. Choi, S. D. Bader, A. A. Parizzi, H. Ambaye, and V. Lauter, Magnetic structure in Fe/Sm-Co exchange spring bilayers with intermixed interfaces, Phys. Rev. B **83**, 174418 (2011).

[36] H. Schultheiss, J. E. Pearson, S. D. Bader, and A. Hoffmann, Thermoelectric detection of spin waves, Phys. Rev. Lett. **109**, 237204 (2012).

[37] B. F. Miao, S. Y. Huang, D. Qu, and C. L. Chien, Inverse spin Hall effect in a ferromagnetic metal, Phys. Rev. Lett. **111**, 066602 (2013).

[38] A. Tsukahara *et al.*, Self-induced inverse spin Hall effect in permalloy at room temperature, Phys. Rev. B **89**, 235317 (2014).

[39] V. Vlaminck, J. E. Pearson, S. D. Bader, and A. Hoffmann, Dependence of spin-pumping spin Hall effect measurements on layer thicknesses and stacking order, Phys. Rev. B **88**, 064414 (2013).

[40] O. Mosendz *et al.*, Detection and quantification of inverse spin Hall effect from spin pumping in permalloy/normal metal bilayers, Phys. Rev. B **82**, 214403 (2010).

[41] K. Ando *et al.*, Optimum condition for spin-current generation from magnetization precession in thin film systems, Appl. Phys. Lett. **94**, 152509 (2009).

[42] T. Wakamura, K. Ohnishi, Y. Niimi, and Y. Otani, Large spin accumulation with long spin diffusion length in Cu/MgO/permalloy lateral spin valves, Appl. Phys. Express. **4**, 063002 (2011).

[43] X. Fan, H. Celik, J. Wu, C. Ni, K-J. Lee, V. O. Lorenz, and J. Q. Xiao, Quantifying interface and bulk contributions to spin-orbit torque in magnetic bilayers, Nature Commun. **5**, 3042 (2014).

[44] L. Vila, T. Kimura, and Y. Otani, Evolution of the spin Hall effect in Pt nanowires: Size and temperature effects, Phys. Rev. Lett. **99**, 226604 (2007).

[45] S. Meyer, M. Althammer, S. Geprags, M. Opel, R. Gross, and S. T. B. Goennenwein, Temperature dependent spin transport properties of platinum inferred from spin Hall magnetoresistance measurements, Appl. Phys. Lett. **104**, 242411 (2014).

[46] G. Y. Guo, S. Murakami, T.-W. Chen, and N. Nagaosa, Intrinsic spin Hall effect in platinum: First-principles calculations, Phys. Rev. Lett. **100**, 096401 (2008).

[47] Y. M. Lu *et al.*, Pt magnetic polarization on $Y_3Fe_5O_{12}$ and magnetotransport characteristics, Phys. Rev. Lett. **110**, 147207 (2013).

[48] T. Lin *et al.*, Experimental investigation of the nature of the magnetoresistance effects in Pd-YIG hybrid structures, Phys. Rev. Lett. **113**, 037203 (2014).

[49] J. P. Perdew, K. Burke, and M. Ernzerhof, Generalized gradient approximation made simple, Phys. Rev. Lett. **77**, 3865 (1996).

[50] See http://www.flapw.de.

[51] N. Marzari, A. A. Mostofi, J. R. Yates, I. Souza, and D. Vanderbilt, Maximally localized Wannier functions: Theory and applications, Rev. Mod. Phys. **84**, 1419 (2012).

[52] F. Freimuth, Y. Mokrousov, D. Wortmann, S. Heinze, and S. Blügel, Maximally localized Wannier functions within the FLAPW formalism, Phys. Rev. B **78**, 035120 (2008).

[53] A. A. Mostofi, J. R. Yates, Y.-S. Lee, I. Souza, D. Vanderbilt, and N. Marzari, A tool for obtaining maximally-localised Wannier functions, Comput. Phys. Commun. **178**, 685 (2008).

[54] H. J. Monkhorst and J. D. Pack, Special points for Brillouin-zone integrations, Phys. Rev. B **13**, 5188 (1976).

[55] H.-R. Fuh *et al.*, Intrinsic anomalous Hall effect in nickel: A GGA + U study, Phys. Rev. B **84**, 144427 (2011).